

## Ion Beam Instabilities during Solar Flare Energy Release

A. Fitzmaurice,<sup>1, a)</sup> J. F. Drake,<sup>1, b)</sup> and M. Swisdak<sup>1, c)</sup>

*Institute for Research in Electronics and Applied Physics,  
University of Maryland, College Park, Maryland 20742,  
USA*

(Dated: 28 January 2025)

The linear stability of waves driven by ion beams produced during solar flare energy release are explored to assess their role in driving abundance enhancements in minority species such as  $^3\text{He}$  and in controlling, through pitch-angle scattering, proton/alpha confinement during energy release. The Arbitrary Linear Plasma Solver (ALPS) is used to solve the linear dispersion relation for a population of energetic, reconnection-accelerated protons streaming into a cold background plasma. We assume equal densities of the two populations, using an anisotropic ( $T_{\parallel}/T_{\perp} = 10$ ), one-sided kappa distribution for the energetic streaming population and a cold Maxwellian for the background. We find two unstable modes with parallel propagation: a right-handed wave with a frequency of the order of the proton cyclotron frequency ( $\Omega_{cp}$ ) and a left-handed, lower frequency mode. We also find highly oblique modes with frequencies below  $\Omega_{cp}$  that are unstable for higher beam energies. Through resonant interactions, all three modes will contribute to the scattering of the high-energy protons, thereby limiting their transport out of the flare-acceleration region. The higher-frequency oblique mode, which can be characterized as a kinetic Alfvén wave, will preferentially heat  $^3\text{He}$ , making it a good candidate for the driver of the abundance enhancements commonly observed for this species in impulsive events.

---

<sup>a)</sup>Electronic mail: [afitz@umd.edu](mailto:afitz@umd.edu)

<sup>b)</sup>Electronic mail: [drake@umd.edu](mailto:drake@umd.edu)

<sup>c)</sup>Electronic mail: [swisdak@umd.edu](mailto:swisdak@umd.edu)

## I. INTRODUCTION

In collisionless plasmas such as the solar wind and solar corona, velocity distributions frequently exhibit non-Maxwellian features that can trigger the growth of plasma waves. Free energy is converted into heat as particles are scattered by these waves through resonant interactions. This has recently been observed by Parker Solar Probe in the solar wind, where ion-scale wave activity concurrent with proton beams led to scattering of the beams in velocity space perpendicular to the background magnetic field.<sup>1,2</sup>

The linear theory of ion beam instabilities using Maxwellian distributions has been explored extensively. Much of the early work<sup>3-7</sup> focused primarily on modes propagating parallel/anti-parallel to the magnetic field, specifically the right-hand polarized mode that is resonant with the beam population. However, Daughton and Gary<sup>8</sup> found additional left-hand polarized oblique modes that are dominant for beams with large densities and moderate drift speeds ( $1 \leq v_D/v_A \leq 2$ , where  $v_A$  is the Alfvén speed). Voitenko and Goossens<sup>9</sup> and Barik, Singh, and Lakhina<sup>10</sup> have also shown that ion beams can generate highly oblique kinetic Alfvén waves (the form of the classic Alfvén wave when  $k_\perp \rho_s = k_\perp c_s/\Omega_{ci} \sim 1$ , where  $k_\perp$  is the perpendicular wavenumber,  $c_s$  is the sound speed, and  $\Omega_{ci}$  is the ion cyclotron frequency<sup>11-13</sup>).

While much of this previous work has focused on the solar wind, ion beam instabilities should also be present during solar flare energy release as accelerated particles interact with less energetic plasma in the corona. Unlike the typical Maxwellians that have been used to identify instabilities in the past, ion energy spectra from both solar energetic particle observations<sup>14,15</sup> and reconnection simulations<sup>16</sup> exhibit non-thermal power-law tails that can extend out to several MeV. These are better modeled by kappa distributions, a difference that can impact the growth rates of linear instabilities.<sup>17</sup>

Waves generated by reconnection-accelerated particles are of particular interest in the case of impulsive solar energetic particle events, which frequently exhibit enhancements of the  $^3\text{He}/^4\text{He}$  abundance ratio by up to a factor of  $10^4$ .<sup>15,18</sup> It is commonly believed that these enhancements are caused by preferential heating and acceleration through cyclotron resonance, due to the unique charge-to-mass ratio of fully ionized  $^3\text{He}$ ,  $q/m = 2/3$  (when normalized to that of protons).<sup>19</sup> However, the source of the waves responsible for this acceleration remains unknown. While many previous theories have focused on electrons as

the driver,<sup>20–23</sup> simulations show that the ions gain more energy during reconnection,<sup>16,24</sup> making them a more likely driver for the waves causing extreme enhancements.

Using particle-in-cell simulations, Fitzmaurice, Drake, and Swisdak<sup>25</sup> (hereafter denoted as FDS) explored the waves generated by flare-accelerated proton and alpha particles, modeled by one-sided kappa distributions streaming into a cold background plasma. The distributions were found to be unstable to parallel, right-handed waves at all beam energies explored and additional left-handed and oblique waves at higher energies. These waves are expected to have a significant impact on the particle dynamics in solar eruptions, as they were shown to both efficiently scatter ion beams into more isotropic distributions and increase the temperatures of  $^3\text{He}$  by a factor of 20. FDS<sup>25</sup> proposed that waves generated by flare-accelerated proton and alpha beams will heat  $^3\text{He}$  in the regions surrounding the flare site. The heated particles will then stream into the flare acceleration region and increase the abundances there, leading to the enhancements commonly observed in impulsive events.

Due to the complexity of the initial distribution functions, FDS<sup>25</sup> did not solve for the linear dispersion relation and instead relied on comparing simulation results to the previous linear analysis done with Maxwellian distributions. In this paper, we use the `Arbitrary Linear Plasma Solver` (ALPS)<sup>26,27</sup> to find the unstable linear wave modes directly from the distributions used in FDS.<sup>25</sup> The method for solving for the linear dispersion relation is explained further in Sec. II, results from ALPS are presented in Sec. III, and we conclude with comparisons to the simulation results from FDS<sup>25</sup> and implications for  $^3\text{He}$  acceleration in Sec. IV.

## II. SOLVING FOR THE LINEAR DISPERSION RELATION

As discussed in Stix<sup>28</sup>, solving for the linear wave modes of a plasma involves finding values of the wave frequency  $\omega$  and wavevector  $\vec{k}$  for which the determinant of the dispersion tensor  $|D|$  goes to zero. In general,  $\omega$  is complex, with  $\text{Re}(\omega) = \omega_r$  corresponding to the real frequency of the wave and  $\text{Im}(\omega) = \gamma$  corresponding to growth ( $\gamma > 0$ ) or damping ( $\gamma < 0$ ) of the mode. We take the components of  $\vec{k}$  to be positive so that the direction of propagation is denoted by the sign of the real frequency.

Each  $\omega$  and  $\vec{k}$  solution has a corresponding eigenvector that gives the electric field components of the mode. In the case of electromagnetic waves, a polarization can be defined

with respect to the background magnetic field. We take  $\vec{B} = B_0 \vec{z}$  so that the polarization is:

$$P = \frac{E_y}{iE_x} \frac{\omega_r}{|\omega_r|}$$

In this case,  $P > 0$  corresponds to right-handed modes and  $P < 0$  corresponds to left-handed modes, with  $P = \pm 1$  corresponding to circular polarization.

Evaluating the integrals required to calculate  $|D|$  can often be difficult. Therefore many numerical solvers approximate the distribution function as a series of Maxwellians or kappa functions, for which the calculations are greatly simplified. However, as shown in Walters *et al.*<sup>29</sup>, these approximations can lead to significant differences in determining the unstable modes of a plasma.

To avoid these issues, ALPS solves for the dispersion relation directly from arbitrary gyrotropic distribution functions. To begin, the distribution functions are discretized in momentum space according to a user-defined grid. The discretized distributions are then used for the numerical integration, including near poles with  $\gamma > 0$ . In the case of poles with  $\gamma \leq 0$ , an analytic continuation is required and the distribution near the poles is approximated using fit functions.

For our analysis, we use the same distribution functions as in FDS.<sup>25</sup> The distribution functions for the protons and alphas (when present) consist of equal densities of a cold, Maxwellian population and a hot, streaming population represented by a one-sided kappa function. We use a 241 x 121 momentum grid with  $-m_i c \leq p_{\parallel} \leq m_i c$  and  $0 \leq p_{\perp} \leq m_i c$ , where  $c = 20v_A$ , and generate the distributions using the function,

$$\begin{aligned} f = & \frac{n_c}{(2\pi m_i T_c)^{3/2}} \exp \left[ \frac{-(p_{\parallel}^2 + p_{\perp}^2)}{2m_i T_c} \right] \\ & + \frac{1}{4} (\tanh(10p_{\parallel}) + 1) (1 - \tanh(10(|\vec{p}| - 0.81m_i c))) \\ & \times \frac{\Gamma(\kappa + 1)}{\Gamma(\kappa - 1/2)(\kappa - 3/2)^{3/2}} \frac{n_{\kappa}}{\sqrt{8\pi^3 m_i^3 T_{\kappa,\perp}^2 T_{\kappa,\parallel}}} \\ & \times \left( 1 + \frac{p_{\parallel}^2}{2m_i(\kappa - 3/2)T_{\kappa,\parallel}} + \frac{p_{\perp}^2}{2m_i(\kappa - 3/2)T_{\kappa,\perp}} \right)^{-(\kappa+1)} \end{aligned} \quad (1)$$

The normalization parameters  $n_c$  and  $n_{\kappa}$  are set to ensure that the background and streaming populations each have densities equal to 0.5 and the tanh functions create cutoffs

at  $p_{\parallel} = 0$  and  $|v|/c = 0.81$ . The latter cutoff, which excludes particles near the speed of light, was necessary to avoid numerical inaccuracies in the PIC simulations but does not affect the linear results. As in FDS,<sup>25</sup> we consider three initial energies for the streaming population. In Case 1,  $T_{\kappa,\parallel} = 10m_p v_A^2$ . Case 2 has a lower initial energy, with  $T_{\kappa,\parallel} = 5m_p v_A^2$ , and Case 3 has a higher initial energy, with  $T_{\kappa,\parallel} = 20m_p v_A^2$ . In all cases,  $\kappa = 2.5$ ,  $T_{\kappa,\parallel}/T_{\kappa,\perp} = 10$  and the Maxwellian population has a temperature  $T_c = 0.1m_p v_A^2$ . Proton distributions are shown in Figure 1. In all cases, the distribution for the electrons is a Maxwellian with  $T_e = 2m_p v_A^2$  and a small drift to balance the current.

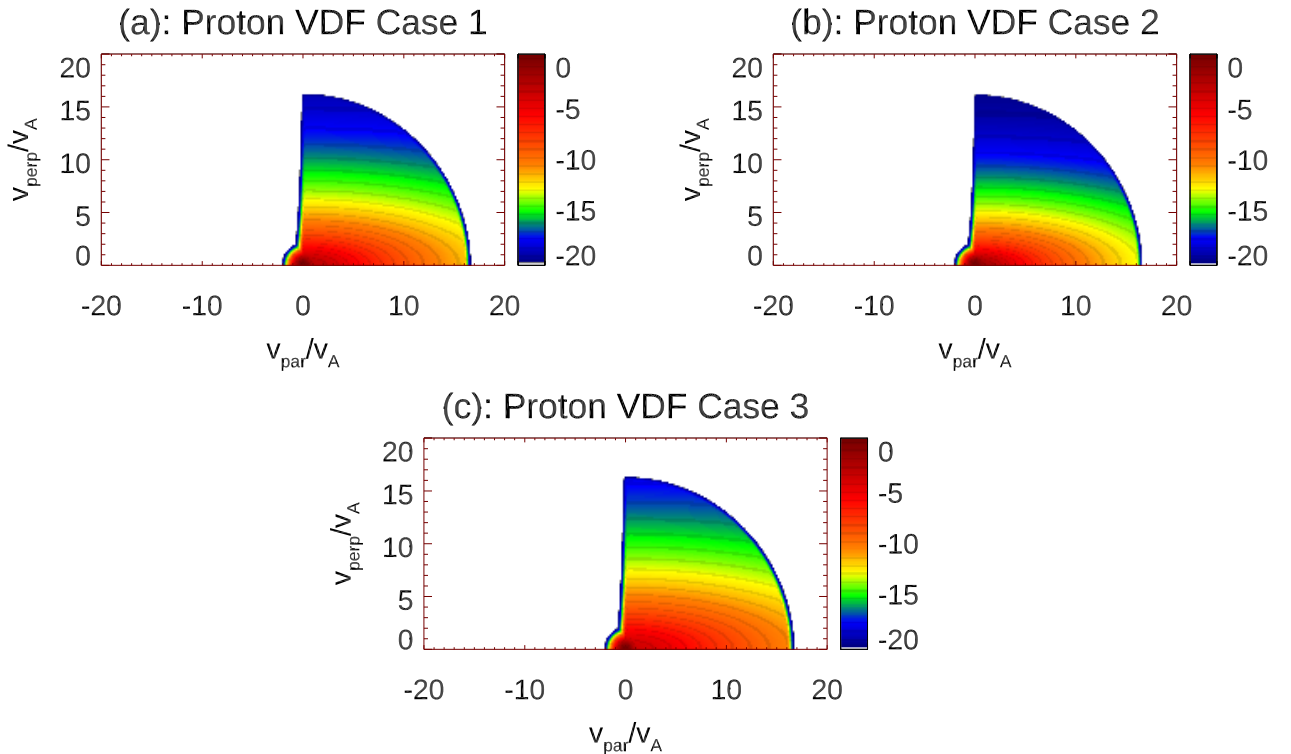


FIG. 1. The velocity ( $v_{\parallel}$  vs.  $v_{\perp}$ ) distribution functions used by ALPS for the protons in (a) Case 1, (b) Case 2, and (c) Case 3. The beam energy is lower in Case 2 than in Case 1 and is higher in Case 3. All distributions are plotted on the same logarithmic scale.

We initially consider just protons and electrons, so that the number densities are  $n_p = n_e = 1$ . We then add the alphas at 5% the proton number density, so that  $n_p = 1$ ,  $n_{\text{Alpha}} =$

0.05, and  $n_e = 1.1$ . For all species, the distributions are treated as non-relativistic and the fit functions used in the numerical integration are the analytic functions used to generate the distributions.

### III. RESULTS

#### A. Parallel Modes

We begin our analysis by looking for the unstable  $\vec{k} \times \vec{B} = 0$  modes for Case 1 in an electron-proton plasma. To do this, ALPS first calculates  $|D(\omega_r, \gamma)|$  in the range  $\omega_r/\Omega_{cp} = [-0.25, 0.25]$  and  $\gamma/\Omega_{cp} = [-0.1, 0.2]$  for  $k_{\parallel}d_p = 0.1$  (Fig. 2(a)). After identifying any roots with  $\gamma > 0$ , ALPS performs root-finding scans over  $k_{\parallel}d_p = [0.1, 1]$  to determine the dispersion properties of each mode (Fig. 2(b)-(d)). For each solution along the wavenumber scan, the components of the wave electric field are also calculated to determine the polarization.

In Case 1, we find two unstable parallel modes for  $k_{\parallel} = 0.1$ , located at  $(\omega_r/\Omega_{cp}, \gamma/\Omega_{cp}) = (0.23, 0.14)$  and  $(0.065, 0.11)$ . The first, higher frequency mode is a right-hand circularly polarized wave that is non-dispersive with  $\omega_r/k = 2.5v_A$ . It is unstable over the full range of  $k_{\parallel}$  and has a peak growth rate of  $\gamma/\Omega_{cp} = 0.19$  at  $k_{\parallel}d_p = 0.27$ . The second, lower frequency mode is a left-hand circularly polarized wave that is dispersive, with the frequency plateauing around  $0.2\Omega_{cp}$  before becoming stable above  $k_{\parallel}d_p = 0.6$ . The mode reaches a peak growth rate of  $\gamma/\Omega_{cp} = 0.18$  at  $k_{\parallel}d_p = 0.32$ ,  $\omega_r/\Omega_{cp} = 0.17$ .

Changing the initial energy of the streaming population primarily affects the lower frequency, left-handed mode. In the lowest energy case, this mode becomes stable everywhere except for a small range around  $k_{\parallel}d_p = 0.13$  (Fig. 3(b)). In the highest energy case, it becomes the dominant mode and is strongly unstable for all values of  $k_{\parallel}$ , with a peak growth rate of  $\gamma/\Omega_{cp} = 0.33$  at  $k_{\parallel}d_p = 0.48$  (Fig. 4(b)). There is a modest impact on the right-handed mode as the initial energy is changed, with growth rates and real frequencies increasing with beam energy. However, the overall characteristics of the mode remain the same across the three cases.

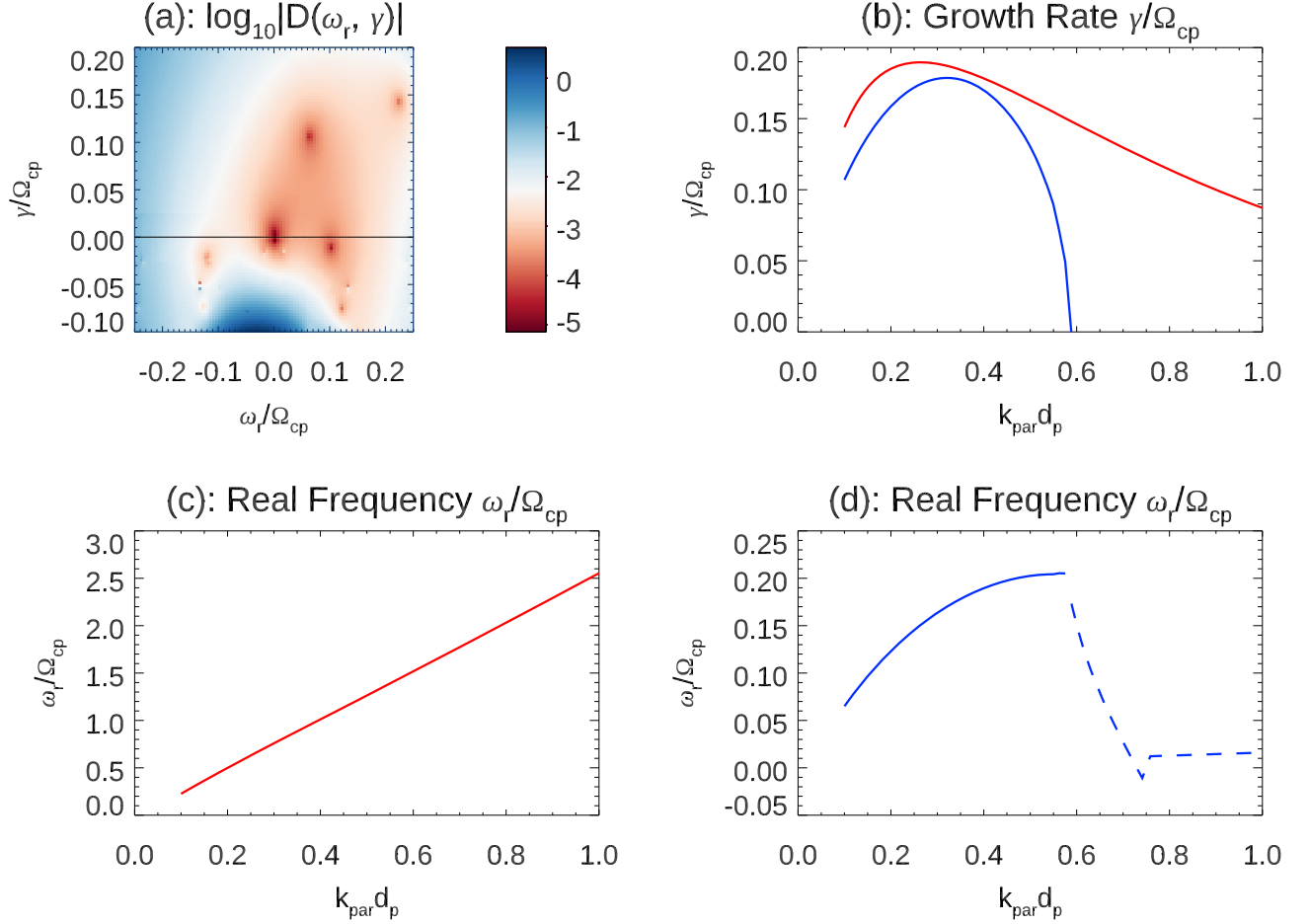


FIG. 2. (a) The map of  $|D(\omega_r, \gamma)|$  for Case 1 at  $k_{\parallel} = 0.1$ ,  $k_{\perp} = 10^{-4}$ , with minima plotted in dark red. The right-handed mode is located at  $(\omega_r/\Omega_{cp}, \gamma/\Omega_{cp}) = (0.23, 0.14)$  and the left-handed mode is located at  $(\omega_r/\Omega_{cp}, \gamma/\Omega_{cp}) = (0.065, 0.11)$ . The (b) growth rates and (c)-(d) real frequencies of the two unstable solutions are plotted as functions of  $k_{\parallel}$ , with the right-handed mode plotted in red and the left-handed mode plotted in blue. Real frequencies while the mode is unstable are plotted as a solid line, while real frequencies while the mode is stable are plotted as a dashed line.

## B. Oblique Modes

Using the same method as described for the parallel case, we also find the unstable modes with  $\vec{k} \times \vec{B} \neq 0$ . In Case 1, as  $k_{\perp}$  increases from 0, the growth rates for the two unstable parallel modes drop off quickly and the lightly damped mode located at  $(\omega_r/\Omega_{cp}, \gamma/\Omega_{cp}) = (0.1, -0.01)$  in Fig. 2(a) becomes unstable. It reaches a maximum growth rate of  $\gamma/\Omega_{cp} = 0.18$  around  $k_{\parallel}d_p = 0.28$ ,  $k_{\perp}d_p = 1$ ,  $\omega_r/\Omega_{cp} = 0.49$  (Fig. 5), becoming stable

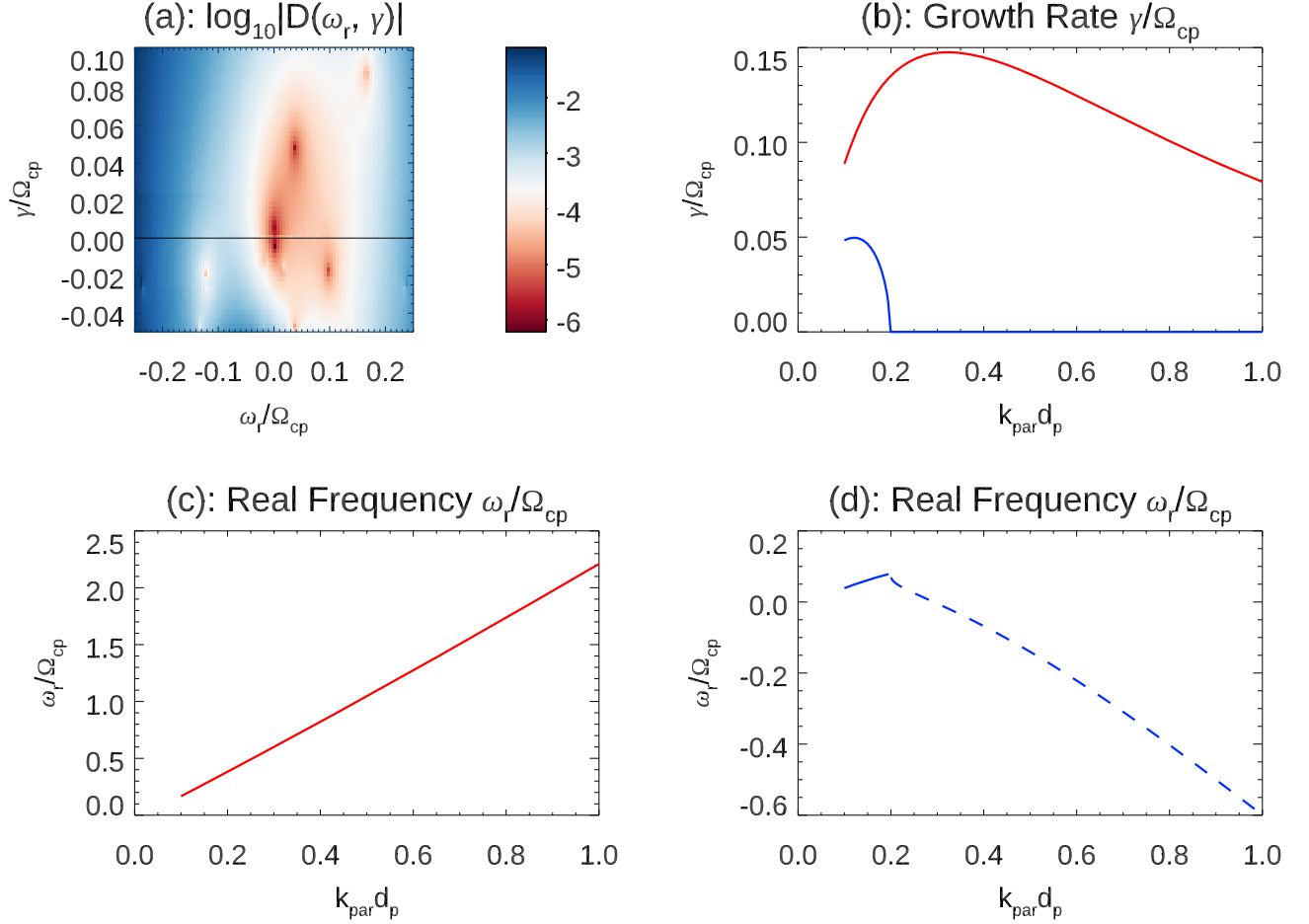


FIG. 3. (a) The map of  $|D(\omega_r, \gamma)|$  for Case 2 at  $k_{\parallel} = 0.1$ ,  $k_{\perp} = 10^{-4}$ , with minima plotted in dark red. The right-handed mode is located at  $(\omega_r/\Omega_{cp}, \gamma/\Omega_{cp}) = (0.17, 0.089)$  and the left-handed mode is located at  $(\omega_r/\Omega_{cp}, \gamma/\Omega_{cp}) = (0.039, 0.048)$ . The (b) growth rates and (c)-(d) real frequencies of the two unstable solutions are plotted as functions of  $k_{\parallel}$ , with the right-handed mode plotted in red and the left-handed mode plotted in blue. Real frequencies while the mode is unstable are plotted as a solid line, while real frequencies while the mode is stable are plotted as a dashed line.

above  $k_{\parallel}d_p = 0.6$ . The growth rate is large over a broad range of  $k_{\perp}$  and  $\partial\omega_r/\partial k_{\perp}$  is small around peak growth. At  $k_{\perp} = 0$ , the mode is electrostatic. However, for  $k_{\perp} \neq 0$ , it gains an electromagnetic component. The electromagnetic field is strong for long wavelengths ( $|k|d_p < 1$ ), but weakens as  $k_{\perp}$  increases. At maximum growth, the energy in the electric field transverse to  $\vec{k}$  compared to the total wave electric field is  $E_T^2/E^2 = 0.28$  and the mode is predominately linearly polarized in the perpendicular direction. The increase in the frequency at large  $k_{\perp}$  combined with its electromagnetic (electrostatic) character at long

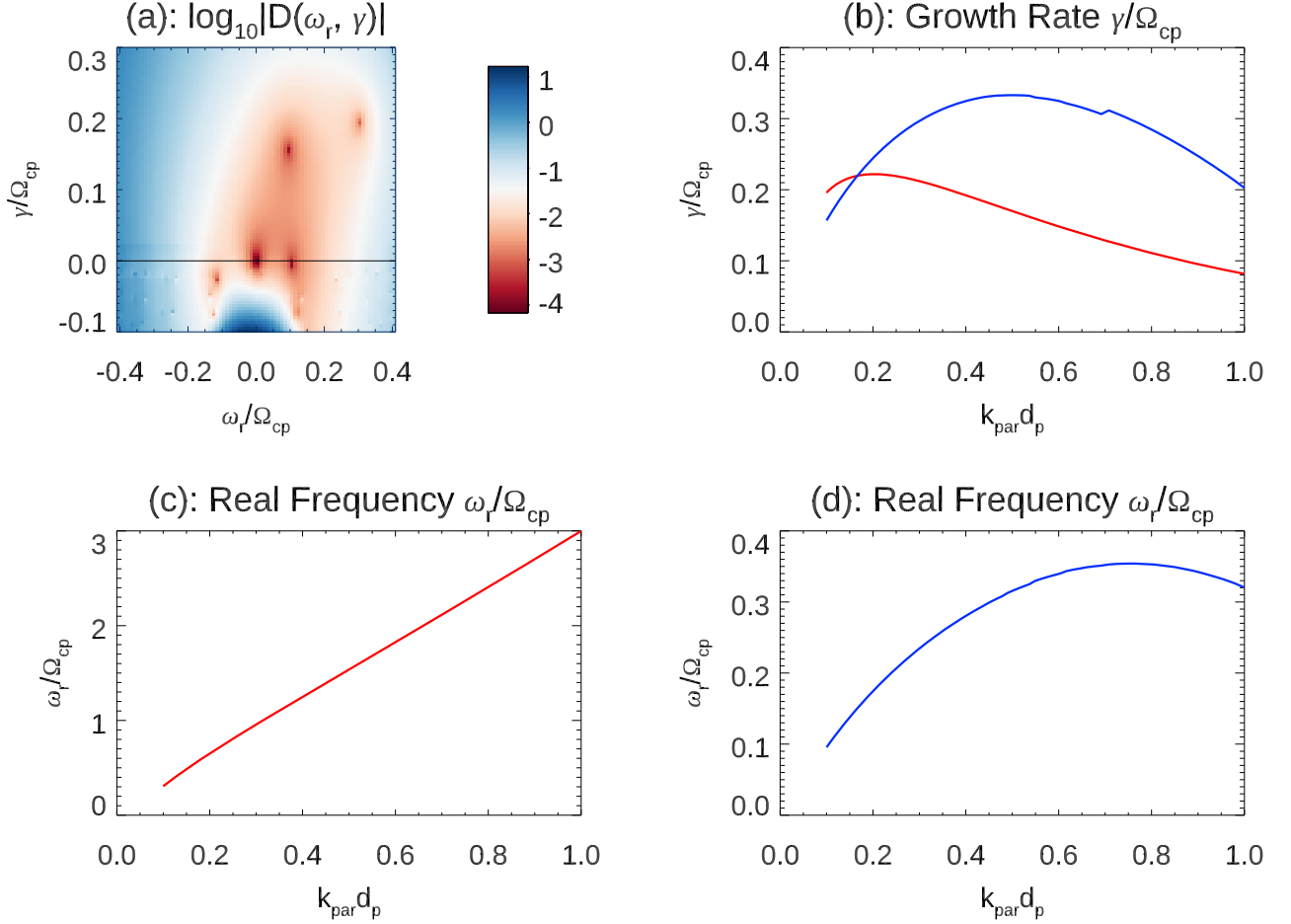


FIG. 4. (a) The map of  $|D(\omega_r, \gamma)|$  for Case 3 at  $k_{\parallel} = 0.1$ ,  $k_{\perp} = 10^{-4}$ , with minima plotted in dark red. The right-handed mode is located at  $(\omega_r/\Omega_{cp}, \gamma/\Omega_{cp}) = (0.31, 0.20)$  and the left-handed mode is located at  $(\omega_r/\Omega_{cp}, \gamma/\Omega_{cp}) = (0.096, 0.16)$ . The (b) growth rates and (c)-(d) real frequencies of the two unstable solutions are plotted as functions of  $k_{\parallel}$ , with the right-handed mode plotted in red and the left-handed mode plotted in blue.

(short) wavelength suggest that this instability can be characterized as a kinetic Alfvén wave.

Lowering the initial energy decreases both the growth rate and obliquity of this mode, which, for Case 2, has a maximum growth rate of  $\gamma/\Omega_{cp} = 0.11$  around  $k_{\parallel}d_p = 0.23$ ,  $k_{\perp}d_p = 0.5$ ,  $\omega_r/\Omega_{cp} = 0.31$  (Fig. 6). Raising the particle energy increases the growth rate, reaching a maximum value of  $\gamma/\Omega_{cp} = 0.25$  at  $k_{\parallel}d_p = 0.26$ ,  $k_{\perp}d_p = 1$ ,  $\omega_r/\Omega_{cp} = 0.52$  in Case 3 (Fig. 7(a)-(b)). In both cases, the value of  $E_T^2/E^2$  at peak growth is the same as in Case 1.

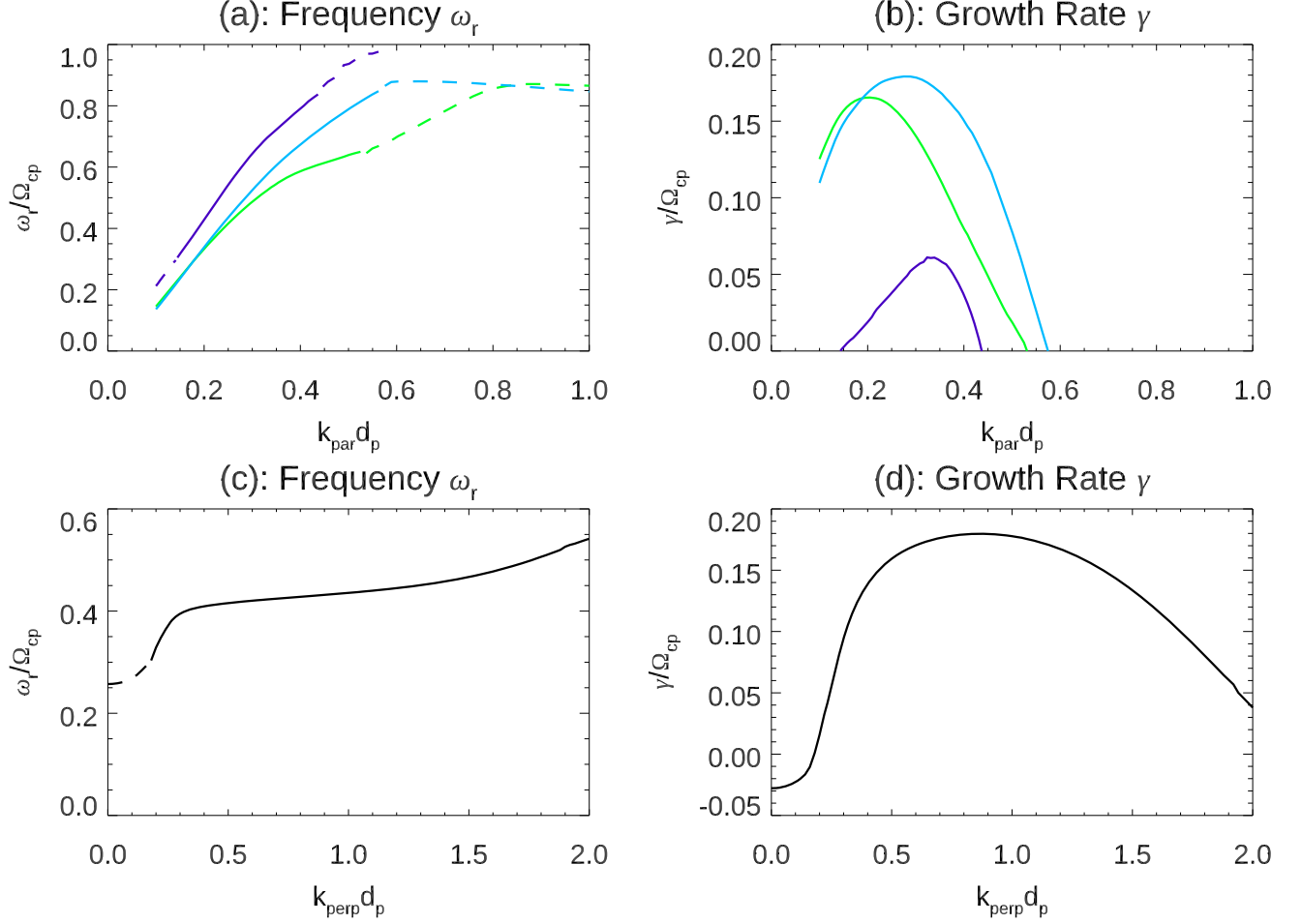


FIG. 5. The dispersion properties for the oblique mode in Case 1. The top two plots show, as a function  $k_{\parallel}$ , the (a) frequencies and (b) growth rates for  $k_{\perp} d_p = 0.5$  (green), 1 (blue), and 2 (purple). Real frequencies while the mode is unstable are plotted as a solid line, while real frequencies while the mode is stable are plotted as a dashed line. The bottom two plots show, as a function of  $k_{\perp}$ , the (c) frequency and (d) growth rate for  $k_{\parallel} = 0.25$ .

In the highest energy case, there are also significant growth rates for the left-handed mode discussed in Sec. III A for  $k_{\perp} \neq 0$  (Fig. 7(c)-(d)). Although the parallel wavenumber associated with the peak growth rate increases as  $k_{\perp}$  increases, the other characteristics of the mode remain the same as in the  $k_{\perp} = 0$  case.

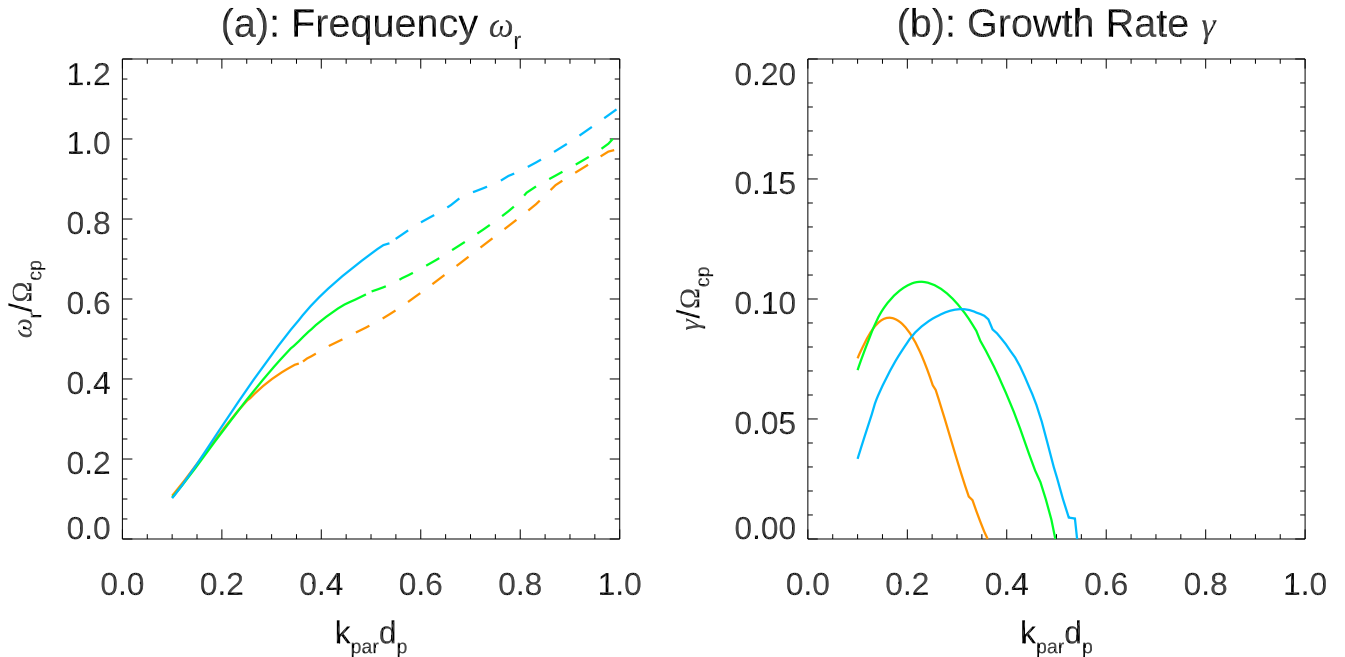


FIG. 6. The dispersion properties for the oblique mode in Case 2. The plots show, as a function of  $k_{\parallel}$ , the (a) frequencies and (b) growth rates for  $k_{\perp} d_p = 0.25$  (orange),  $0.5$  (green), and  $1$  (blue). Real frequencies while the mode is unstable are plotted as a solid line, while real frequencies while the mode is stable are plotted as a dashed line.

### C. Impact of ${}^4\text{He}$

In order to test the impact of  ${}^4\text{He}$  on the spectrum of modes, we repeat the linear analysis while including a population of  ${}^4\text{He}$  with a number density equal to 5% that of the protons, reflecting typical abundances in the corona. The initial distribution functions are given by Eq. 1, with the same temperatures in each case as the protons. As a representative example, the frequencies and growth rates of the unstable modes for Case 1 are shown in Figure 8 (parallel modes) and Figure 9 (oblique modes). Since there is very little difference between these results and those presented in the previous sections, we conclude that, at the

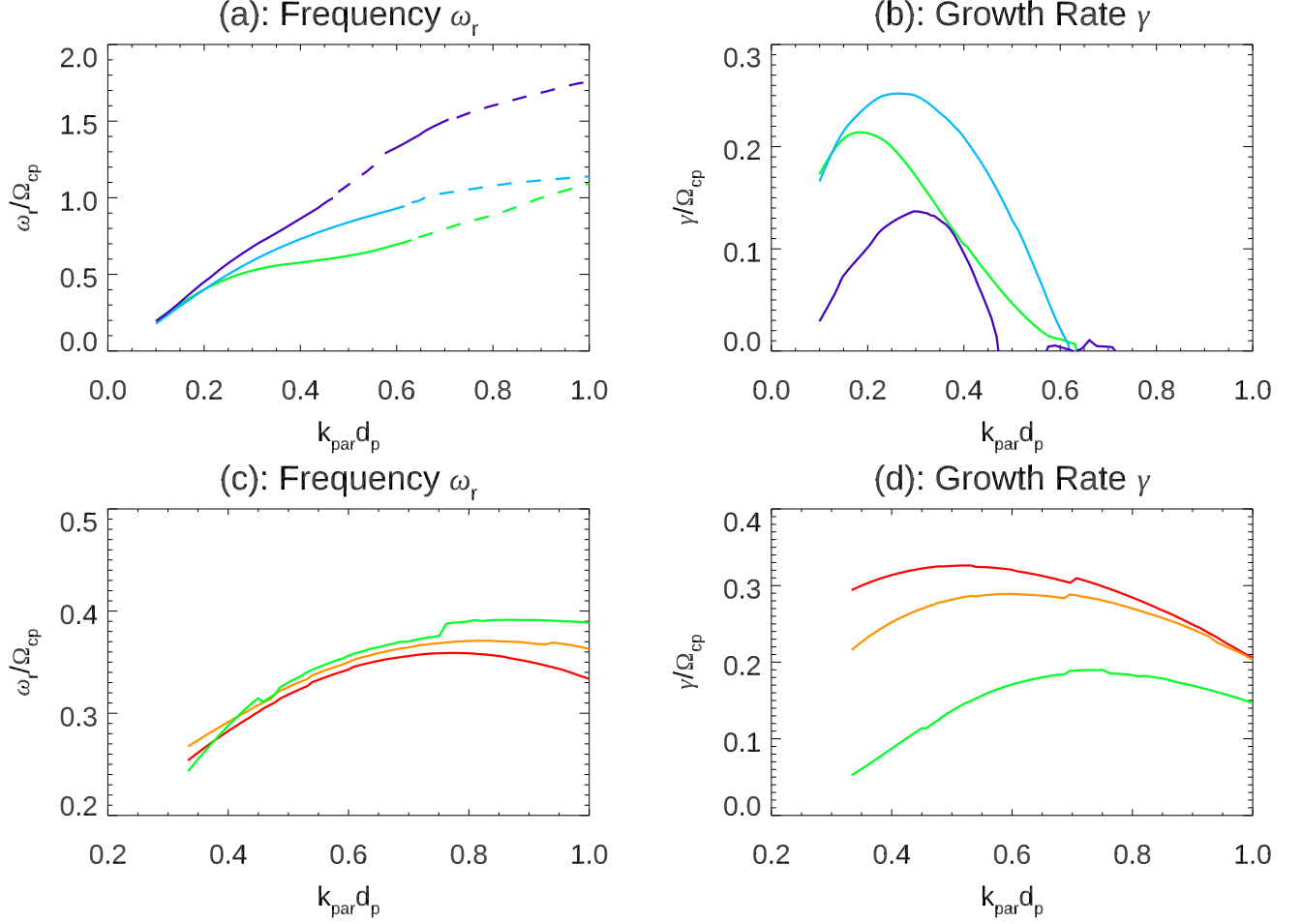


FIG. 7. The dispersion properties for both oblique modes in Case 3. The top two plots show, as a function of  $k_{\parallel}$ , the (a) frequencies and (b) growth rates for  $k_{\perp} d_p = 0.5$  (green), 1 (blue), and 2 (purple) of the linearly polarized mode. Real frequencies while the mode is unstable are plotted as a solid line, while real frequencies while the mode is stable are plotted as a dashed line. The bottom two plots show, as a function of  $k_{\parallel}$ , the (c) frequencies and (d) growth rates for  $k_{\perp} d_p = 0.1$  (red), 0.25 (orange), and 0.5 (green) of the left-hand polarized mode.

low densities expected in the corona, this species has little impact on the generation of ion beam-driven instabilities.

#### IV. DISCUSSION

The linear theory results from ALPS are in good agreement with the simulation results presented in FDS.<sup>25</sup> The linear parallel right-handed mode that is unstable in all cases is

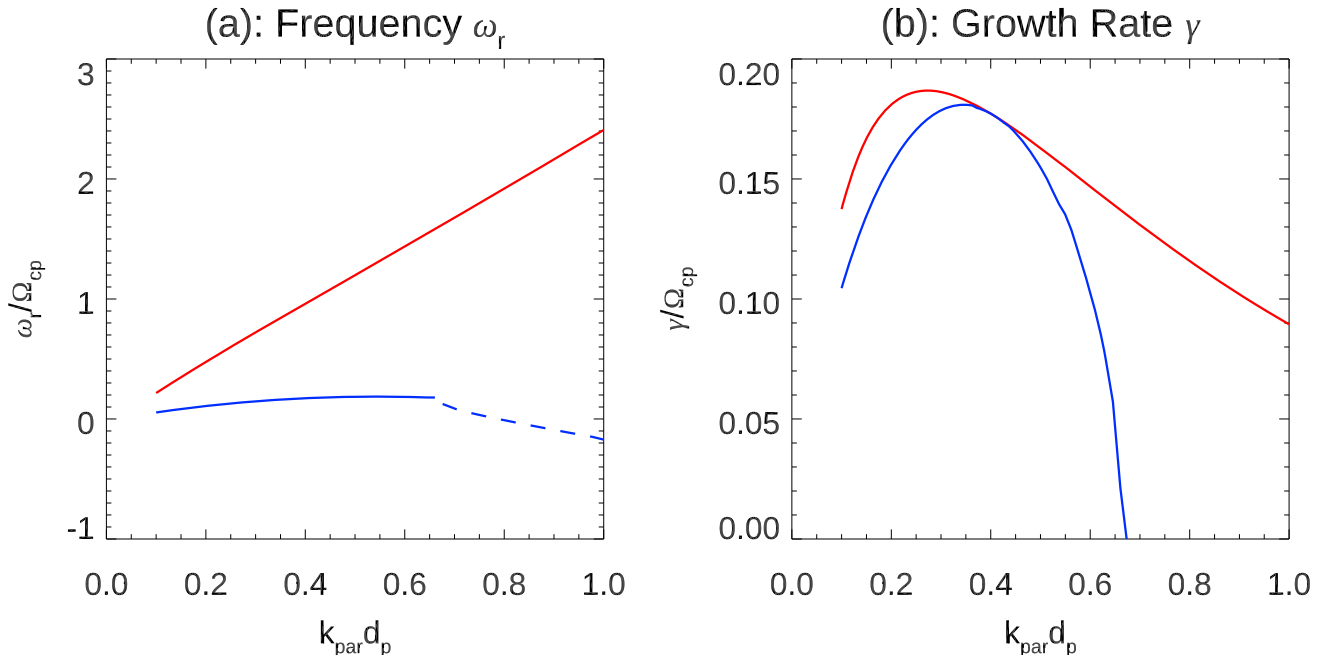


FIG. 8. The (a) frequencies and (b) growth rates as a function of  $k_{\parallel}$  for the parallel modes in Case 1 including a  ${}^4\text{He}$  number density equal to 5% that of the protons (compare to Fig. 2 with no  ${}^4\text{He}$ ). The right-hand polarized mode is plotted in red and the left-handed mode is plotted in blue. Real frequencies while the mode is unstable are plotted as a solid line, while real frequencies while the mode is stable are plotted as a dashed line.

the primary cause for the parallel waves observed in the simulations for Cases 1 and 2 and at late time for Case 3. It is most likely a form of the right-hand resonant instability that is well documented for ion beams (see Sec. I).

The large growth rates for the left-handed mode in Case 3 lead to the higher parallel wavenumbers and mixed polarity observed at early time in the simulations for this case. It is less certain if it can be identified with any of the instabilities previously discussed in the literature. Given that the growth rates are strongly dependent on the beam energy and that the mode remains unstable for oblique wavevectors, it appears to be similar to the Alfvén

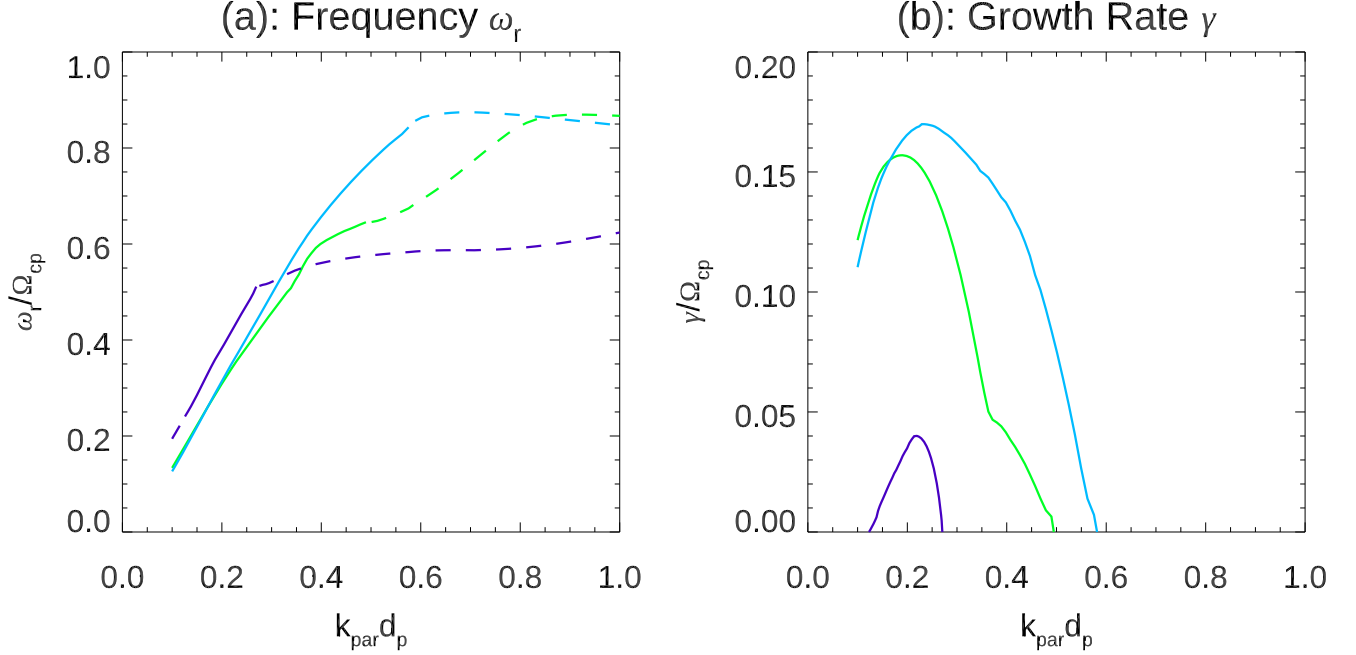


FIG. 9. The (a) frequencies and (b) growth rates as a function of  $k_{\parallel}$  for  $k_{\perp} = 0.5$  (green), 1 (blue), and 2 (purple) in Case 1 including a  ${}^4\text{He}$  number density equal to 5% that of the protons (compare to Fig. 5 with no  ${}^4\text{He}$ ). Real frequencies while the mode is unstable are plotted as a solid line, while real frequencies while the mode is stable are plotted as a dashed line.

instabilities discussed in Daughton and Gary<sup>8</sup>.

In the PIC simulation results of FDS,<sup>25</sup> the waves produced by the distributions in Case 2 are primarily parallel, which is consistent with the smaller linear growth rates for the oblique mode in this case. For Cases 1 and 3, linear theory predicts large growth rates for this mode at nearly perpendicular wavenumbers ( $\approx 75^\circ$ ). This is reproduced well in the simulation results for both cases at early time. The mode is most likely a kinetic Alfvén wave, since the electromagnetic field is strong in the long wavelength limit but weakens as  $k_{\perp} d_p \sim k_{\perp} \rho_s$  approaches 1.

According to the linear theory, interactions between the waves and the ions will occur

when the velocity of a particle is equal to the resonant velocity,  $v_r = (\omega_r \pm n\Omega_{cp})/k_{\parallel}$ , where the plus sign corresponds to electrostatic and right-hand polarized waves and the minus sign to left-handed waves. In the case of parallel propagation for electrostatic waves,  $n = 0$  and the resonant velocity equals the phase velocity of the wave, so that wave-particle interactions only occur through the Landau resonance. For parallel propagating electromagnetic waves,  $n = 1$ ; therefore, interactions occur at the cyclotron resonance, which is above (below) the phase velocity for right-handed (left-handed) waves. For all wave modes at oblique propagation, there are an infinite number of resonant velocities ( $n = 0, \pm 1, \pm 2, \dots$ ), both above and below the phase velocity of the wave.

From the linear resonance condition, all three instabilities will be important for proton and alpha scattering during solar energy release. The parallel right-handed mode and the positive resonances of the kinetic Alfvén wave will scatter particles in the high energy tail of the distribution, reducing their parallel energy and converting it into perpendicular energy. The parallel left-handed mode and the negative resonances of the kinetic Alfvén wave will scatter particles into negative parallel velocities, contributing to thermalization of the distribution. The strong scattering of protons and alpha particles resulting from these instabilities will cause these particles to diffuse rather than free-stream along the magnetic field within the flaring region. This will greatly increase the time required for them to escape from the flare energy release region and therefore extend the time over which particles can gain energy, which will facilitate greater energy gain.

Heating cold  $^3\text{He}$  requires a resonance at  $v_{\parallel} = 0$ , which is not possible for the parallel right-handed mode due to the positive definite numerator in  $v_r$  when  $\omega_r > 0$ . For the parallel left-handed mode, this would require  $\omega_r/\Omega_{cp} = 2/3$ , which is much higher than the frequencies predicted for this mode by the linear theory (see Figs. 2-4). The kinetic Alfvén wave will contribute to  $^3\text{He}$  heating through the  $n = -1$  resonance, since it has unstable frequencies near the resonance frequency of  $^3\text{He}$ :  $\omega_r/\Omega_{cp} = 2/3$  (see Figs. 5-7).

However, wave heating of  $^3\text{He}$  is not limited to those waves with  $\omega_r/\Omega_{cp} = 2/3$ . As discussed in Temerin and Roth<sup>20</sup> and FDS,<sup>25</sup> the frequencies of waves traveling through the corona will remain constant while the cyclotron frequencies of the constituent ion species will change with the magnetic field strength, according to  $\Omega_{ci} = qB/mc$ . Therefore, waves with frequencies  $1/2 < \omega_r/\Omega_{cp} < 2/3$  will heat  $^3\text{He}$  above the flare site where  $|B|$  is smaller. For  $\omega_r/\Omega_{cp} < 1/2$ , other ion species will dominate absorption compared with  $^3\text{He}$  because

of the latter’s small number density. Waves with frequencies  $2/3 < \omega_r/\Omega_{cp} < 1$  will heat  ${}^3\text{He}$  below the flare site where  $|B|$  is larger. Frequencies above this range will be absorbed by protons. Because of their increased thermal speeds, heated  ${}^3\text{He}$  ions can then migrate back into the energy release site, increasing their local abundance. Within the flaring region this  ${}^3\text{He}$  will be further accelerated to high energy by the usual Fermi reconnection drive mechanism<sup>16</sup>. From the linear theory results for Cases 1 and 3, the frequencies at peak growth are in the range  $1/2 < \omega_r/\Omega_{cp} < 1$ , so there should be substantial energy in this frequency range to heat  ${}^3\text{He}$ . Since the addition of  ${}^4\text{He}$  had little effect on the linear analysis, we conclude that kinetic Alfvén waves driven by reconnection-accelerated protons streaming out from energy release sites are a strong candidate for driving the  ${}^3\text{He}$  enhancements seen in impulsive events.

## V. ACKNOWLEDGMENTS

The authors were supported by NSF grant PHY2109083, NASA grants 80NSSC20K1813 and 80NSSC20K1277, and NASA FINESST award 80NSSC23K1625. This study benefits from discussions within the International Space Science Institute (ISSI) Team ID 425 “Origins of 3He-rich SEPs.” We acknowledge informative discussions with Drs. R. Bucik and G. Mason. ALPS can be found at [github.com/danielver02/ALPS](https://github.com/danielver02/ALPS) and assistance in using the code was provided by Dr. K. Klein.

## VI. AUTHOR DECLARATIONS

### A. Conflicts of Interest

The authors have no conflicts to disclose.

### B. Author Contributions

**A. Fitzmaurice:** Conceptualization (supporting); formal analysis (lead); funding acquisition (equal); investigation (lead); methodology (equal); visualization (lead); writing—original draft (lead); writing—review and editing (equal). **J. F. Drake:** Conceptualization (lead); formal analysis (supporting); funding acquisition (equal); methodology

(equal); project administration (lead); supervision (lead); writing–original draft (supporting); writing–review and editing (equal). **M. Swisdak**: Conceptualization (supporting); formal analysis (supporting); funding acquisition (equal); methodology (equal); supervision (supporting); writing–original draft (supporting); writing–review and editing (equal).

## VII. DATA AVAILABILITY

The data that support the findings of this study are available from the corresponding author upon reasonable request.

## REFERENCES

- <sup>1</sup>J. L. Verniero, D. E. Larson, R. Livi, A. Rahmati, M. D. McManus, P. S. Pyakurel, K. G. Klein, T. A. Bowen, J. W. Bonnell, B. L. Alterman, P. L. Whittlesey, D. M. Malaspina, S. D. Bale, J. C. Kasper, A. W. Case, K. Goetz, P. R. Harvey, K. E. Korreck, R. J. MacDowall, M. Pulupa, M. L. Stevens, and T. D. de Wit, “Parker Solar Probe Observations of Proton Beams Simultaneous with Ion-scale Waves,” *The Astrophysical Journal Supplement Series* **248**, 5 (2020).
- <sup>2</sup>J. L. Verniero, B. D. G. Chandran, D. E. Larson, K. Paulson, B. L. Alterman, S. Badman, S. D. Bale, J. W. Bonnell, T. A. Bowen, T. D. de Wit, J. C. Kasper, K. G. Klein, E. Lichko, R. Livi, M. D. McManus, A. Rahmati, D. Verscharen, J. Walters, and P. L. Whittlesey, “Strong Perpendicular Velocity-space Diffusion in Proton Beams Observed by Parker Solar Probe,” *The Astrophysical Journal* **924**, 112 (2022).
- <sup>3</sup>M. D. Montgomery, S. P. Gary, D. W. Forslund, and W. C. Feldman, “Electromagnetic Ion-Beam Instabilities in the Solar Wind,” *Physical Review Letters* **35**, 667–670 (1975).
- <sup>4</sup>M. D. Montgomery, S. P. Gary, W. C. Feldman, and D. W. Forslund, “Electromagnetic instabilities driven by unequal proton beams in the solar wind,” *Journal of Geophysical Research (1896-1977)* **81**, 2743–2749 (1976).
- <sup>5</sup>S. P. Gary, C. W. Smith, M. A. Lee, M. L. Goldstein, and D. W. Forslund, “Electromagnetic ion beam instabilities,” *The Physics of Fluids* **27**, 1852–1862 (1984).
- <sup>6</sup>S. P. Gary, “Electromagnetic ion/ion instabilities and their consequences in space plasmas: A review,” *Space Science Reviews* **56**, 373–415 (1991).

- <sup>7</sup>S. P. Gary, *Theory of Space Plasma Microinstabilities* (Cambridge University Press, 1993).
- <sup>8</sup>W. Daughton and S. P. Gary, “Electromagnetic proton/proton instabilities in the solar wind,” *Journal of Geophysical Research: Space Physics* **103**, 20613–20620 (1998).
- <sup>9</sup>Y. Voitenko and M. Goossens, “Excitation of high-frequency Alfvén waves by plasma outflows from coronal reconnection events,” *Solar Physics* **206**, 285–313 (2002).
- <sup>10</sup>K. C. Barik, S. V. Singh, and G. S. Lakhina, “Kinetic Alfvén waves generated by ion beam and velocity shear in the Earth’s magnetosphere,” *Physics of Plasmas* **26**, 022901 (2019).
- <sup>11</sup>A. Hasegawa, “Kinetic properties of Alfvén waves,” *Proceedings of the Indian Academy of Sciences - Section A* **86**, 151–174 (1977).
- <sup>12</sup>J. V. Hollweg, “Kinetic Alfvén wave revisited,” *Journal of Geophysical Research: Space Physics* **104**, 14811–14819 (1999).
- <sup>13</sup>J. S. Zhao, Y. Voitenko, M. Y. Yu, J. Y. Lu, and D. J. Wu, “PROPERTIES OF SHORT-WAVELENGTH OBLIQUE ALFVÉN AND SLOW WAVES,” *The Astrophysical Journal* **793**, 107 (2014).
- <sup>14</sup>D. V. Reames, L. M. Barbier, a. T. T. V. Rosenvinge, G. M. Mason, J. E. Mazur, and a. J. R. Dwyer, “Energy Spectra of Ions Accelerated in Impulsive and Gradual Solar Events,” *The Astrophysical Journal* **483**, 515 (1997).
- <sup>15</sup>G. M. Mason, “<sup>3</sup>He-Rich Solar Energetic Particle Events,” *Space Science Reviews* **130**, 231–242 (2007).
- <sup>16</sup>Z. Yin, J. F. Drake, and M. Swisdak, “Simultaneous Proton and Electron Energization during Macroscale Magnetic Reconnection,” *The Astrophysical Journal* **974**, 74 (2024).
- <sup>17</sup>S. M. Shaaban, M. Lazar, R. A. López, and S. Poedts, “Electromagnetic Ion–Ion Instabilities in Space Plasmas: Effects of Suprathermal Populations,” *The Astrophysical Journal* **899**, 20 (2020).
- <sup>18</sup>D. V. Reames, “Particle acceleration at the Sun and in the heliosphere,” *Space Science Reviews* **90**, 413–491 (1999).
- <sup>19</sup>L. A. Fisk, “<sup>3</sup>He-rich flares: a possible explanation.” *The Astrophysical Journal* **224**, 1048–1055 (1978).
- <sup>20</sup>M. Temerin and I. Roth, “The Production of <sup>3</sup>He and Heavy Ion Enrichments in <sup>3</sup>He-rich Flares by Electromagnetic Hydrogen Cyclotron Waves,” *The Astrophysical Journal* **391**, L105 (1992).

- <sup>21</sup>I. Roth and M. Temerin, “Enrichment of 3He and Heavy Ions in Impulsive Solar Flares,” *The Astrophysical Journal* **477**, 940 (1997).
- <sup>22</sup>T. X. Zhang, “Solar 3He-rich Events and Electron Acceleration in Two Stages,” *The Astrophysical Journal* **518**, 954 (1999).
- <sup>23</sup>G. Paesold, R. Kallenbach, and A. O. Benz, “Acceleration and Enrichment of 3He in Impulsive Solar Flares by Electron Firehose Waves,” *The Astrophysical Journal* **582**, 495 (2003).
- <sup>24</sup>J. P. Eastwood, T. D. Phan, J. F. Drake, M. A. Shay, A. L. Borg, B. Lavraud, and M. G. G. T. Taylor, “Energy Partition in Magnetic Reconnection in Earth’s Magnetotail,” *Physical Review Letters* **110**, 225001 (2013).
- <sup>25</sup>A. Fitzmaurice, J. F. Drake, and M. Swisdak, “Wave Generation by Flare-accelerated Ions and Implications for 3He Acceleration,” *The Astrophysical Journal* **964**, 97 (2024).
- <sup>26</sup>D. Verscharen, K. G. Klein, B. D. G. Chandran, M. L. Stevens, C. S. Salem, and S. D. Bale, “ALPS: the Arbitrary Linear Plasma Solver,” *Journal of Plasma Physics* **84**, 905840403 (2018).
- <sup>27</sup>K. G. Klein, D. Verscharen, T. Koskela, and D. Stansby, “danielver02/alps: Zenodo release. version 1.0.1,” <https://doi.org/10.5281/zenodo.8075682> (2023).
- <sup>28</sup>T. H. Stix, *Waves in Plasmas* (American Institute of Physics Melville, NY, 1992).
- <sup>29</sup>J. Walters, K. G. Klein, E. Lichko, M. L. Stevens, D. Verscharen, and B. D. G. Chandran, “The Effects of Nonequilibrium Velocity Distributions on Alfvén Ion-cyclotron Waves in the Solar Wind,” *The Astrophysical Journal* **955**, 97 (2023).